1368R2

A mechanism for Nb incorporation in rutile and application of Zr-in-rutile thermometry: A case study from granulite facies paragneisses of the Mogok metamorphic belt, Myanmar

MAW MAW WIN[1, *], M. ENAMI[2, †], T. KATO[2] AND YE KYAW THU[1]

[1] Department of Earth and Planetary Sciences, Graduate School of Environmental Studies, Nagoya University, Nagoya 464-8601, Japan

[2] Institute for Space–Earth Environmental Research, Nagoya University, Nagoya 464-8601, Japan

* Present address: Yadanabon University, Amarapura, Mandalay, Myanmar

† E-mail: enami@nagoya-u.jp

Running Title: Nb incorporation in rutile and application of Zr-in-rutile thermometry

Mineralogical Magazine (2017) 81, 1503–1521.

ABSTRACT

Rutile grains extensively occur in host phases of biotite and quartz-feldspar aggregate in high-temperature paragneisses of the Mogok metamorphic belt of Myanmar. They occur as an isolated phase and sometimes show intergrowth texture with ilmenite. Most rutile grains contain up to 3.7 wt% Nb_2O_5, which shows positive correlations with Fe a2013 trivalent elements. Niobium substitutes for Ti by a coupled substitution with the trivalent cations (M^{3+}) of $Nb^{5+}M^{3+}Ti^{4+}_{-2}$. Fine-grained rutile grains included in ilmenite are distinctly poor in Nb (< 0.1 wt% as Nb_2O_5) and contain Fe of 1.7–3.2 wt% as Fe_2O_3, suggesting vacancy-bearing substitution of $Fe^{3+}_4Ti^{4+}_{-3}\square_{-1}$, where $\square$ indicates a vacancy. The rutile grains in the felsic phases contain high Zr contents up to 4200 ppm, suggesting equilibrium temperatures over 800 °C by the Ti-in-rutile geothermometer. These high-temperature conditions are consistent with those estimated by conventional methods reported in the literature and suggest wide occurrences of the upper-amphibolite and granulite facies metamorphic rocks in the middle segment of the Mogok metamorphic belt. In contrast, the Zr contents of rutile grains in biotite are usually less than 1000 ppm, implying equilibrium temperatures lower than 750 °C. Most of the Zr-poorer rutile grains might have been included in biotite and were isolated from the zircon-bearing system during an early stage of prograde metamorphism. Some other Zr-poorer rutile grains might have been an exsolved phase from Ti-rich biotite during retrograde metamorphism, which was furthered by the infiltration of metamorphic fluid under lower-amphibolite facies conditions.

KEYWORDS: Niobium, Zirconium, Rutile, Mogok metamorphic rock, Myanmar

Introduction

Rutile is a dominant reservoir of some high field strength elements (HFSEs) (e.g., Foley *et al.*, 2000; Klemme *et al.*, 2005; Bowles *et al.*, 2011). Zack *et al.* (2002) estimated that rutile grains in an eclogite from Trescolmen, Central Alps concentrated >90 % of Ti, Nb, Sb, Ta, and W and 5–45 % of V, Cr, Mo, and Sn of the whole-rock contents. Khodos *et al.* (1988) synthetically showed that rutile is in a solid solution with up to 25 mol % Nb under 1400 °C. Additionally, they concluded that (1) small amounts of Nb less than 3 mol % generally substitute into the rutile structure in a pentavalent state, and (2) Nb-richer rutile contains Nb in a quadrivalent state, suggesting that the rutile structure contains NbO_2-TiO_2 solutions. Natural occurrences of Nb-rich rutile are reported mainly in pegmatites (~27.7 wt% as Nb_2O_5: Černý *et al.*, 1999; Černý and Chapman, 2001), kimberlites (~20.9 wt%: Tollo and Haggerty, 1987), and eclogite xenoliths (~11.3 wt%: Sobolev *et al.*, 2011; Korolev *et al.*, 2014; Hirtopanu *et al.*, 2015) and pyrope crytals (~15.6 wt%: Rezvukhin *et al.*, 2016) in kimberlites. Nb-bearing rutile occurs rarely in common metamorphic rocks, and Dymek (1983) reported rutile grains with 3.1–5.0 wt% Nb_2O_5 in cordierite-anthophyllite-garnet gneisses in the Malene supracrustal rocks from West Greenland.

Rutile shows a strong temperature dependence on Zr substitution, and experimental results and observations on rocks suggest that the Zr content in rutile, when equilibrated with quartz and zircon, should be a useful thermometer for metamorphic rocks (Zack *et al.*, 2004; Watson *et al.*, 2006; Ferry and Watson 2007; Tomkins *et al.*, 2007; Ewing *et al.*, 2013; Pape *et al.*, 2016). Rutile grains containing Zr over 7000 ppm were reported from granulite facies metamorphic rocks (e.g., Zack *et al.*, 2004; Meyer *et al.*, 2011; Pape *et al.*, 2016), functioning as an important Zr reservoir under high-temperature

conditions. Villaseca *et al.* (2007) estimated that rutile could contain 10–35 % of the whole-rock content of Zr in the cases of peraluminous granulites from Spanish Central System (SCS) batholith.

Maw Maw Win *et al.* (2016) briefly reported an occurrence of Nb-rich rutile (~3.7 wt% Nb_2O_5) in a paragneiss from the Sagaing ridge of the Mogok metamorphic belt, Myanmar. They also described that the Zr content of the rutile in the Sagaing paragneisses reached 3600 ppm, implying a high-temperature equilibrium over 850 °C. Additional, systematic, and more precise analyses, including Cr, V, and other minor elements have been carried out on rutile grains in the Sagaing paragneisses for discussion of the mechanism of Nb incorporation in rutile and the application of Zr-in-rutile thermometry. In this study, we (1) report the results of systematic analyses of Nb, Zr, and other trace elements of rutile grains in the Mogok metamorphic rocks from the Sagaing ridge, (2) discuss possible substitution mechanisms of Nb into rutile, and (3) describe the relationship between Zr contents and modes of occurrence of rutile, which might be understood by equilibria during prograde and retrograde metamorphic systems.

Outline of geology and sample description

Rutile-bearing samples in this study were collected from the Sagaing ridge of the Mogok metamorphic belt in Myanmar. Myanmar and the surrounding regions are composed of Western and Eastern provinces bordered by the 1200 km long and N–S trending right-lateral Sagaing fault (Fig. 1a). The Western province is composed of the Burma microplate and a part of the Indochina region (e.g. Mitchell *et al.*, 2007). The Eastern province belongs to the Sibumasu block of the Asian plate. The Mogok

93 metamorphic belt lies along the western margin of the Eastern province. Yonemura *et al.*
94 (2013), Maw Maw Win *et al.* (2016), and Ye Kyaw Thu *et al.* (2016, 2017) reported
95 equilibrium conditions of 0.6–1.0GPa/780–950°C for paragneisses using conventional
96 geothermobarometries, and suggested that high-temperature metamorphic rocks of
97 upper amphibolite and granulite facies extensively occur in the Mandalay and Mogok
98 regions in the central Mogok metamorphic belt. The main event of metamorphism was
99 regarded to be Paleogene or younger (Bertrand *et al.*, 1999; Searle *et al.*, 2007;
100 Yonemura *et al.*, 2013; Maw Maw Win *et al.*, 2016). Maw Maw Win *et al.* (2016)
101 reported calculated chemical Th–U–total Pb isochron method (CHIME) monazite ages
102 in the Late Eocene and Late Oligocene epochs, which were interpreted as the peak
103 metamorphic stage of upper-amphibolite and/or granulite facies and the postdated
104 hydration stage, respectively.
105 The geological and petrographical characteristics of the Mogok metamorphic rocks of
106 the Sagaing ridge were well described by Maw Maw Win *et al.* (2016). The main
107 metamorphic rocks in the Sagaing ridge are paragneiss, mafic gneiss, amphibolite,
108 calc-silicate rock, and marble. The Sagaing ridge is divided into the Sagaing
109 Metamorphic Unit 1 (SM1) and Sagaing Metamorphic Unit 2 (SM2), which are
110 paragneiss-dominant units, mainly intercalating amphibolite and calc-silicate
111 rock/marble layers, respectively (Fig. 1b). Paragneisses, in which the rutile grains were
112 studied, are a major lithology of the Sagaing ridge and are mainly composed of garnet,
113 biotite, plagioclase, K-feldspar, sillimanite, quartz, and minor amounts of rutile,
114 ilmenite, zircon, and graphite. Among the six paragneiss samples discussed in this study,
115 S26, S28, and S30 belong to the SM1 unit, and S22a, S22b, and S36 belong to the SM2

unit (Fig. 1b). Mineral assemblages and compositional characteristics of garnet, biotite, and plagioclase of the analyzed samples are listed in Table 1.

Whole-rock compositions

Major and trace element compositions of three samples, S22a, S22b, and S26 were determined by an X-ray fluorescence spectrometer (XRF; Rigaku ZSX Primus II equipped with an Rh X-ray tube operated at 60 kV and 50 mA) at Nagoya University. These elements were calibrated using standard rock samples issued by the Geological Survey of Japan (GSJ) (Geochemical Reference Sample Data Base, https://gbank.gsj.jp/geostandards/welcome.html) and composite standards prepared by Yamamoto and Morishita (1997).

The whole-rock compositions of three paragneisses are listed in Table 2. The data of a paragneiss, which was collected from an outcrop in calc silicate marble-dominant area of the Onzon area in the Mogok metamorphic belt (longitude 96°06≠043 E, latitude 22°48≠423 N: Ye Kyaw Thu *et al.*, 2017), is also listed for comparison. The paragneiss (S26) alternating with amphibolite layers of the SM1 unit is lower in SiO_2 (51.7 wt%) and higher in (FeO* + MnO + MgO) (17.6 wt%) contents than those occurring as layers with calc-silicate rocks/marble in the SM2 unit (S22a and S22b: 62.6–67.5 wt% and 10.4–10.5 wt%). The Al_2O_3 content is distinctly higher in S26 (18.6 wt%) than in S22a and S22b (12.6–14.9 wt%). The Onzon paragneiss contains whole-rock composition similar to the samples S22a and S22b.

Mineralogical characteristics

Analytical procedures

Quantitative chemical analyses and X-ray mapping of the rutile and coexisting ilmenite were carried out using a JEOL JCXA-8800R (WDS + EDS) and JCXA-733 electron-probe microanalyzers (EPMA) at Nagoya University. The accelerating voltage, specimen current, and beam diameter for quantitative analyses were 15 kV, 12 nA on the Faraday cup, and 2–3 μm, respectively. Well-characterized natural and synthetic phases were employed as standards. The matrix correction was performed by using the α-factor table of Kato (2005). The interference of TiKβ to VKα was corrected for the quantitative analysis of V in rutile. The detection limits (2σ level) of Nb_2O_5, Ta_2O_5, and Zr are 0.04 wt%, 0.10 wt% and 300 ppm, respectively. The representative analyses of the rutile and ilmenite grains are listed in Table 3.

Modes of occurrence and chemical compositions of rutile

The rutile grains occur in host phases of biotite (Figs. 2a and b) and quartz–feldspar aggregates (Figs. 2c and d), and are texturally divided into an isolated grain (Figs. 2b, c, and d) and intergrowth grain with ilmenite (Figs. 2a and d). The isolated and intergrowth types of rutile grains occur both in biotite and the felsic phases. These rutile grains are textually homogeneous and do not show any lines of evidence for re-equilibrium such as exsolutions of zircon needles and baddeleyite lamellae and Zr-compositional zoning (Fig. 2). The total iron contents are usually less than 1.2 wt% as Fe_2O_3 in most samples (Fig. 3). These two types of rutile grains occur in samples S26, S28, and S36, and the intergrowth grains tend to be richer in Fe than the coexisting isolated grains in each sample. Although, the Nb_2O_5 contents are usually less than 0.8 wt%, those in samples S26, S36, and S22a reach 3.7 wt%, 1.5 wt%, and 1.3 wt%, respectively (Fig. 4). The Cr_2O_3 and V_2O_3 contents reach 0.25 and 0.86 wt%,

164 respectively, and show no difference due to the host phases and textures of the rutile
165 grains (Fig. 5). The rutile grains in the felsic phases are rich in Zr (2080 ± 610 – 3100 ±
166 250 ppm), and those in biotite have a distinctly lower Zr content (480 ± 150 – 830 ± 300
167 ppm) (Fig. 6).
168 In sample S26, small grains of rutile (15-35 μm in size) occur as an aggregate
169 included by ilmenite (Nbf-Rt in Figs. 2a and 7a). These grains are distinctly poorer in
170 Nb_2O_5 (less than 0.1 wt%: Fig. 4) and characteristically richer in iron (1.7–3.2 wt% as
171 Fe_2O_3: Fig. 3) than the other coexisting rutile grains of the intergrowth type (0.27–3.7
172 wt% Nb_2O_5 and 0.3–1.3 wt% Fe_2O_3), and will be denoted as "Nb-free and Fe-rich
173 rutile" hereafter. They are poor in Cr_2O_3 (less than 0.05 wt%), V_2O_3 (less than 0.09
174 wt%), and Zr (below the detection limit) contents.
175 The Al_2O_3, MnO, and MgO contents of rutile grains of the isolated and intergrowth
176 types are generally less than 0.3, 0.1, and 0.05 wt%, respectively. The Ta_2O_5 content is
177 below the detection limit, and Sb and W, which are also considered to be compatible
178 with the rutile structure (Meinhold, 2010), were not detected by the qualitative analysis.
179
180 *Other phases*
181 The mineralogical characteristics of major phases in the samples S22a, S22b, and S26
182 were described in detail by Maw Maw Win *et al.* (2016). Samples S28, S30, and S36
183 have mineral assemblages and mineral compositions similar to these samples. Garnet
184 grains belong to an almandine–pyrope series with minor grossular and spessartine
185 components ($Alm_{54–78}Prp_{14–41}Sps_{1–5}Grs_{3–7}$: Maw Maw Win *et al.*, 2016; this study).
186 They show a zonal structure with a homogeneous core and an almandine and
187 spessartine-richer and pyrope-poorer thin mantle of 200–600 μm in thickness. Biotite

grains are characteristically rich in TiO_2 with maximum contents from 4.0 wt% of sample S30 to 6.2 wt% of sample S22b (Table 1). Fluorine contents reach 0.9, 1.0, 2.0, 0.4, 0.2, and 1.0 wt% in samples S22a, S22b, S26, S28, S30, and S36, respectively. Plagioclase grains show a zonal structure with a homogeneous core mantled by a less calcic rim, and their maximum calcic compositions range from An_{35} in sample S30 to An_{59} in sample S26. Ilmenite grains have near end-member compositions with Al_2O_3 < 0.04 wt%, Cr_2O_3 < 0.10 wt%, V_2O_3 < 0.05 wt%, MnO = 0.3–2.1 wt% and MgO = 0.05–1.9 wt% (Table 3). The Nb_2O_5 content is usually less than 0.1 wt%, and the Ta_2O_5 content is below the detection limit.

Discussion

Nb and Fe substitutions

Nb-bearing rutile

The rutile grains in the Sagaing paragneisses characteristically show solid solutions with Nb and Fe, suggesting a coupled substitution of these two elements. The rutile grains in sample S26 especially have wide variations of Nd_2O_5 (~3.7 wt%) and Fe (~3.2 wt% as Fe_2O_3), and were used to suggest a mechanism for Nb incorporation in rutile. The whole-rock composition of sample S26 indicates that this sample has a determinably higher Nb content (29 ppm: Table 2) than other common Mogok metamorphic rocks (13–18 ppm) and typical cratonic shales (11–19 ppm: Condie, 1993) including the "North American shale composite" (NASC) (Gromet *et al.*, 1984) and "Post-Archean Australian average shale" (PAAS) (Taylor and McLennan, 1988). The Nb-rich characteristic of the whole-rock composition probably promoted the formation of the Nb-rich rutile.

212 The rutile grains in samples S26 occur as isolated grains in felsic phases and
213 intergrowth grains with ilmenite in biotite (Fig. 2a). The Nb-rich rutile occurs as the
214 core of a zoned grain and is surrounded by a Nb-poor mantle (Figs. 7 and 8). This grain
215 shows intergrowth texture with ilmenite. The Nb content shows positive correlations
216 with the contents of iron and trivalent elements, suggesting coupled substitutions of
217 these elements with Ti.
218 Two possible Nb-bearing substitutions into the rutile structure, $M^{3+}Nb^{5+}Ti^{4+}_{-2}$ and
219 $M^{2+}Nb^{5+}_2Ti^{4+}_{-3}$, where M^{3+} and M^{2+} represent the trivalent and divalent cations,
220 respectively, were proposed (e.g. Vlassopoulos *et al.*, 1993; Černý *et al.*, 1999). The
221 Nb-rich rutile of sample S26 contains Al_2O_3 (up to 0.25 wt%), Cr_2O_3 (up to 0.21 wt%),
222 V_2O_3 (up to 0.61 wt%), and iron (up to 1.3 wt% as Fe_2O_3); therefore, the Nb content
223 might be controlled mainly by the M^{3+}-bearing substitution or a combination of the
224 M^{3+}- and M^{2+}-bearing substitutions. Iron is the only candidate for controlling the
225 M^{2+}-bearing substitution, because the divalent cations such as Zn, Mg, and Mn are least
226 compatible with rutile (e.g., Meinhold, 2010) and were not detected in most of the rutile
227 grains in the Sagaing paragneisses studied (detection limits are about 0.02–0.03 wt% at
228 the 2σ level). Figure 9 illustrates the covariations between the trivalent cations and Nb'
229 (= $Nb^{5+} – 2\ M^{2+}$), where Nb' indicates the niobium content that incorporates into the
230 rutile structure by substitutions other than $M^{2+}Nb^{5+}_2Ti^{4+}_{-3}$. When iron in the rutile
231 structure is presumed to be in a trivalent state (Fig. 9a), the contents of the total trivalent
232 cations and the Nb' show strong positive correlations (correlation coefficient $R^2 = 0.94$).
233 In contrast, if the total iron is treated as being in a divalent state (Fig. 9b), the Nb' values
234 are usually negative and do not show compositional trends implying any type of
235 substitution. Additionally, the number of total cations for O = 2, calculated assuming

236 total iron as Fe_2O_3, are near unity [1.002 ± 0.002 atom per formula unit (apfu): cf. Table
237 3], implying lower amounts of FeO. Therefore, most of iron in the Nb-bearing rutile is
238 assumed to be Fe^{3+}, and the Nb probably incorporates into the rutile structure by a
239 coupled substitution with M^{3+}s, including Fe^{3+}.
240 The Nb-bearing rutile grains generally contain small but non-negligible amounts of
241 excess M^{3+} over Nb'. Such an excess of trivalent cations over the pentavalent cations
242 has been discussed using the data of Nb- and Cr-rich rutile grains from the upper mantle
243 by Vlassopoulos *et al.* (1993). An increasing of the estimated Fe^{2+}/Fe^{3+} value
244 conversely causes a decrease in the Nb'/M^{3+} value as illustrated with an arrow in Fig. 9a
245 (also compare Figs. 9a and b). Therefore the observed excess M^{3+} content over Nb'
246 could not be explained by an overestimation of the Fe^{3+} content and might be due to
247 Nb-free and Fe^{3+}-bearing substitution as will be discussed in the following section for
248 the case of Nb-free and Fe-rich rutile grains included in ilmenite in sample S26 (Fig.
249 2a).
250 Figure 10 shows a strong negative correlation between the Ti and Nb" ($= Nb^{5+} + M^{3+}$)
251 values in Nb-rich rutile grains (inclination = -0.99 and $R^2 = 0.99$), when total iron is
252 assumed to be Fe^{3+}. The combination of the negative Ti–Nb" (Fig. 10) and positive
253 M^{3+}–Nb' (Fig. 9a) correlations clearly suggest that the Nb incorporation into the rutile
254 grains of the Sagaing paragneisses is largely controlled by the following substitution:
255 $$2\ Ti^{4+} = Nb^{5+} + M^{3+}$$
256
257 Nb-free and Fe-rich rutile
258 Nb-free and iron-rich rutile is rare and was reported to occur as a symplectitic phase
259 with magnetite from a mafic-ultramafic layered intrusion in SW China (2.9 wt% as

Fe_2O_3: Tan *et al.*, 2015). Smith and Perseil (1997) compiled and discussed the crystal chemistry of rutile and proposed mechanisms for maintaining the electroneutrality correlated to the substitution of Ti^{4+} by M^{3+} in M^{5+}-free rutile. Vlassopoulos *et al.* (1993) considered that the excess M^{3+} is presumably compensated by H^+ interstitials, which leads to the following substitution:

$$Ti^{4+} + O^{2-} = M^{3+} + (OH)^-$$

This type of substitution was considered as a typical mechanism of Al^{3+} incorporation into titanite (e.g., Smith, 1988; Oberti *et al.*, 1991; Cempírek *et al.*, 2008). The rutile structure shows tunnel sites parallel to the *z* axis; therefore, the Fe^{3+} incorporation into rutile without H^+ is also considered by the following substitution (e.g., Vlassopoulos *et al.*, 1993; Smith and Perseil, 1997):

$$3\ Ti^{4+} + \text{vacancy} = 4\ Fe^{3+}$$

Ferrous iron might substitute into the rutile structure by similar mechanisms as follows:

$$Ti^{4+} + O^{2-}{}_2 = M^{2+} + (OH)^-{}_2$$

$$Ti^{4+} + \text{vacancy} = 2\ Fe^{2+}$$

Figures 11a and b show correlations between Ti and total iron of rutile, assuming Fe^{3+} and Fe^{2+}, respectively. In both cases, vacancy-bearing substitutions explain well the correlations between Ti and iron contents rather than the OH^--bearing substitutions. Additionally, an inclination of Fe^{3+}-Ti correlation (-1.32 : $R^2 = 0.96$) matches with that expected by the substitution of $Fe^{3+}{}_4Ti^{4+}{}_{-3}\square_{-1}$, where $\square$ indicates a vacancy (-1.33: Fig. 11a). There is little evidence to deny the possibility that the rutile contains some amount of ferrous iron by the substitution of $Fe^{2+}{}_2Ti^{4+}{}_{-1}\square_{-1}$. However, the correlation between Ti and Fe^{3+} (Fig. 11a) probably suggests the solid solution towards a pseudorutile

283 component ($Fe^{3+}_2Ti_3O_9$). The excess M^{3+} over Nb estimated in the Nb-bearing rutile
284 (Fig. 9a) might be understood by the $Fe^{3+}_4Ti^{4+}_{-3}\square_{-1}$.
285
286 Coexistence of two types of rutile
287 The Nb-bearing rutile and Nb-free and Fe-rich rutile grains occur as an intergrowth
288 grain in a biotite host (Figs. 2a and 7a). However, they show critical differences in
289 possible substitutions of $Nb^{5+}Fe^{3+}Ti^{4+}_{-2}$ (Fig. 10) and $Fe^{3+}_4Ti^{4+}_{-3}\square_{-1}$ (Fig. 11a),
290 respectively, suggesting diverse mechanisms in their formation. The Nb-bearing rutile
291 grains partly rim ilmenite and are probably formed in equilibrium with ilmenite and/or
292 at slightly later stage than the ilmenite formation. Similar intergrowth textures were
293 reported in low- to medium-grade metasedimentary rocks of the Erzgebirge and were
294 consider to have formed by rutile crystallization from ilmenite (Luvizotto *et al.*, 2009).
295 Another possible mechanism for the rutile formation was the decomposition of Ti-rich
296 biotite, which were reported in granulite facies paragneisses of the Ivrea-Verbano Zone
297 in the Southern Alps (Luvizotto and Zack, 2009). The breakdowns of ilmenite and
298 Ti-rich biotite both progress by prograde metamorphism. Rutile has a distinctly high
299 Nb-partitioning coefficient relative to other solid and melt phases and is a dominant
300 reservoir of Nb (e.g., Zack *et al*., 2002; Meinhold, 2010). Therefore, the rutile zonal
301 structute, showing a concentration of Nb at the ctystal core, has probably formed during
302 the prograde stage, similar to the bell-shaped Mn-zoning of garnet.
303 In contrast, Nb-free and Fe-rich rutile occurs as small grains included by ilmenite,
304 and shows simple Ti-Fe solid solution having a pseudorutile component (Al_2O_3 < 0.06
305 wt%, Cr_2O_3 < 0.05 wt%, V_2O_3 < 0.09 wt%, MnO < 0.05 wt%, and MgO < 0.06 wt%)
306 similar to the surrounding ilmenite (Al_2O_3 < 0.03 wt%, Cr_2O_3 < 0.07 wt%, V_2O_3 < 0.05

wt%, MnO < 0.59 wt%, and MgO < 0.6 wt%). The characteristics of the chemical compositions and mode of occurrence of the Nb-free and Fe-rich rutile grains suggest the possibility that these grains might have formed by exsolution process from the host ilmenite during the retrograde stage.

Zr substitution and temperature estimation

The zirconium contents of rutile grains in the Sagaing paragneisses reach 4200 ppm and are closely related to the host phases of the rutile grains (Fig. 6). Equilibrium temperatures of the rutile grains in felsic phases in the matrix estimated by a Zr-in-rutile geothermometer (Tomkins *et al.*, 2007) are 870 ± 35 °C, 825 ± 45 °C, and 875 ± 10 °C at 0.8 GPa for samples S26 (Fig. 6c), S28 (Fig. 6d), and S30 (Fig. 6e), respectively. These high temperature conditions are consistent with those estimated by conventional geothermobarometries for the Sagaing ridge (0.6–1.0 GPa/780–850 °C: Maw Maw Win *et al.*, 2016), Onzon and Thabeikkyin areas (0.60–0.84GPa/780–860°C: Ye Kyaw Thu *et al.*, 2016, 2017), and Mogok area (0.65–0.87GPa/800–950°C: Yonemura *et al.*, 2013), suggesting wide distributions of the upper amphibolite-granulite facies metamorphic rocks in the central segment of the Mogok metamorphic belt.

In contrast, the rutile grains occurring in biotite show distinctly lower-temperature conditions than those in the felsic phases: 685 ± 30 °C, 695 ± 30 °C, 725 ± 35 °C, and 680 ± 25 °C for samples S22a (Fig. 6a), S22b (Fig. 6b), S26 (Fig. 6c), and S36 (Fig. 6f), respectively. The systematic differences of temperatures between the rutile grains in the hosts of the biotite and felsic phases are also observed in the data for sample S26 (Fig. 6c). Conversely, there is no systematic difference in equilibrium temperatures between rutile phases occurring as isolated grains and intergrowth grains with ilmenite (Fig. 6).

These data imply that the temperature variations retained by the rutile grains might not imply the differences in peak metamorphic conditions among the samples. The bimodal distributions Zr content of rutile grains were well documented from ultra-high temperature metamorphic rocks from the Ivrea Zone, Italy by Pape *et al*. (2016). They texturally grouped the rutile grains into Types I. II, and III. The type I rutile grains are textually homogeneous and show high-temperature equilibria up to 1100 °C. On the other hand, the Type II grains with exsolution needles/lamellae of zircon and baddeleyite and the Type III grains with small zircon crystals at their grain edges usually record lower-temperature conditions down to 600 °C, suggesting re-equilibrium of homogeneous rutile grains during retrograde stage. Pape *et al*. (2016) estimated closure temperature of Zr-redistribution in rutile as about 650–700 °C. In the Sagaing paragneisses, rutile grains in biotite usually show lower-temperature conditions similar to the closure temperature estimated using the Ivrea Zone samples. These rutile grains, however, do not show any re-equilibrium textures such as the cases reported by Pape *et al*. (2016). Therefore, the lower-temperature conditions recorded in some rutile grains of the Sagaing samples are hard to be explained by Zr-redistribution in rutile during retrograde stage.

One possible explanation for the different temperature conditions recorded in the rutile grains might be the differences in the stages at which the rutile was isolated from the zircon-bearing system; that is, the rutile grains in biotite might have been included during an early stage of prograde metamorphism and recorded a lower-temperature condition before the peak metamorphic stage. This interpretation is supported by the Nb zonal structure, which might have formed during prograde recrystallization, retained by the intergrowth-type rutile grains in the sample S26 (cf., Figs. 7 and 8). The estimated

peak metamorphic conditions of over 800 °C probably caused the partial melting of the felsic phases in the matrix (e.g., Maw Maw Win *et al.*, 2016). Therefore, the rutile grains in the aggregates of the felsic phases might have been trapped during solidification after peak temperature and might have recorded the high temperature conditions around the peak metamorphic stage. In samples S22b, S26, and S36, the origin of Zr-poor rutile grains in biotite might be understood by the prograde process.

However, some rutile grains in sample S22a have obviously coexisted with zircon even after they were included by biotite (e.g., Fig. 2b). In such a case, it is hard to explain the Zr-poor composition by isolation of the rutile grain from the zircon-bearing system at an early stage of the prograde metamorphism. An alternative interpretation for the Zr-poor composition of the rutile grains in biotite of sample S22a is that they were later stage products compared to those in the felsic phases during the retrograde stage. The biotite grains in the Sagaing ridge are usually enriched in Ti (~6.2 wt% as TiO_2: cf., Table 1), showing a high-temperature equilibrium. In addition, in sample S22a, the matrix biotite grains that are free from rutile inclusions are rich in TiO_2 up to 5.0 wt%. In contrast, the rutile-bearing biotite grains in the matrix (Fig. 2b) tend to be lower in TiO_2 (3.1–4.0 wt%) (Fig. 12). Additionally, the biotite around the rutile grains is locally depleted in TiO_2 and has higher Mg# [= Mg/(Mg + Fe)] values within a narrow zone of 30–40 μm (Fig. 13). These compositional trends could not be expected to have formed during a prograde metamorphic stage, and the local decrease in Ti observed in sample S22a probably indicates that the Zr-poor rutile formed by an exsolution process during a retrograde stage. The local increase of the Mg# value, however, cannot be explained only by the exsolution of the rutile grains. The potassium content also slightly decreases around the rutile grains, which probably implies leaching of the alkaline elements from

379 the biotite structure during chloritization. Secondary chlorite has a higher Mg# value
380 (0.61–0.64) than its source biotite (0.51–0.59), and, therefore Mg# of biotite is
381 considered to generally increase by chloritization processes. Consequently, the
382 postulated rutile exsolution might have been furthered by the infiltration of
383 metamorphic fluid along the cleavages that also caused weak chloritization. Maw Maw
384 Win *et al.* (2016) reported that the Mogok metamorphic rocks of the Sagaing ridge were
385 recrystallized under amphibolite facies conditions of 0.3–0.5GPa/600–680°C by
386 extensive infiltration of metamorphic fluid. Similar phenomena were reported also in
387 paragneisses of the Onzon and Thabeikkyin areas of the Mogok metamorphic belt (Ye
388 Kyaw Thu *et al.*, 2017) . The lower-temperature conditions (695 ± 30 °C) retained by
389 the Zr-poorer rutile grains in biotite of sample S22b are similar to those estimated for
390 the earlier stage of the retrograde equilibration. These facts might suggest that the
391 lower-temperature rutile grains are more likely to have been products of the retrograde
392 stage.
393
394 **Conclusions**
395 1. The rutile grains occurring in biotite and felsic phases of paragneisses from the
396 Sagaing ridge contain up to 3.7 wt% Nb_2O_5, which is controlled mainly by the
397 coupled substitution $Nb^{5+}Fe^{3+}Ti^{4+}_{-2}$.
398 2. The rutile grains occurring as small aggregate in ilmenite of sample S26 are almost
399 free of Nb_2O_5 and contain a maximum 3.2 wt% iron as Fe_2O_3. This is likely the result
400 of a vacancy site-bearing substitution of $Fe^{3+}_4Ti_{-3}\square_{-1}$, suggesting a solid solution
401 towards a pseudorutile component.

3. The rutile grains in aggregates of the felsic phases are rich in ZrO_2 (~4200 ppm Zr). These grains are considered to have formed at a peak metamorphic stage under granulite facies conditions.

4. The rutile grains in biotite are poorer in ZrO□ (~1500 ppm Zr) than those in the matrix of felsic phases. This type of rutile retains the lower-temperature equilibrium before the peak metamorphic stage or was probably formed by exsolution and/or recrystallization from the Ti-rich biotite with fluid infiltration during a retrograde stage of lower-amphibolite facies.

Acknowledgments

We thank S. Wallis and members of the petrology group of Nagoya University for their participation in numerous discussions. The critical and constructive comments by two anonymous reviewers and M. Arima helped to clarify and improve this manuscript. This research was partially supported by Grant-in-Aids for Scientific Research (ME, 25400511) from the Japan Society for the Promotion of Science (JSPS) and scholarships (MMW and YKY) from Ministry of Education, Culture, Sports, Science and Technology in Japan (MEXT).

References

Bertrand, G., Rangin, C., Maluski, H., Han, T.A., Thein, M., Myint, O., Maw, W. and Lwin, S. (1999) Cenozoic metamorphism along the Shan scarp (Myanmar): evidences for ductile shear along the Sagaing fault or the northward migration of the eastern Himalayan syntaxis? *Geophysical Research Letters*, **26**, 915-918.

Bowles, J.F.W., Howie, R.A., Vaughan, D.J. and Zussman, J. (2011) *Non-silicates : oxides, hydroxides and sulphides (second edition), Rock-Forming Minerals*, **5A**, Pp. 920. The Geological Society, London.

Cempírek, J., Houzar, S. and Novák, M. (2008) Complexly zoned niobian titanite from hedenbergite skarn at Pisek, Czech Republic, constrained by substitutions $Al(Nb,Ta)Ti_{-2}$, $Al(F,OH)(TiO)_{-1}$ and $SnTi_{-1}$. *Mineralogical Magazine*, **72**, 1293-1305.

Černý, P. and Chapman, R. (2001) Exsolution and breakdown of scandian and tungstenian Nb-Ta-Ti-Fe-Mn phases in niobian rutile. *Canadian Mineralogist*, **39**, 93-101.

Černý, P., Chapman, R., Simmons, W.B. and Chackowsky, L.E. (1999) Niobian rutile from the McGuire granitic pegmatite, Park County, Colorado: Solid solution, exsolution, and oxidation. *American Mineralogist*, **84**, 754-763.

Condie, K.C. (1993) Chemical composition and evolution of the upper continental crust: Contrasting results from surface samples and shales. *Chemical Geology*, **104**, 1-37.

Dymek, R.F. (1983) Fe-Ti oxides in the Malene Supracrustals and the occurrence of Nb-rich rutile. *Rapport Grønlands geologiske Undersøgelse*, **112**, 83-94.

Ewing, T.A., Hermann, J. and Rubatto, D. (2013) The robustness of the Zr-in-rutile and

444 Ti-in-zircon thermometers during high-temperature metamorphism
445 (Ivrea-Verbano Zone, northern Italy). *Contributions to Mineralogy and*
446 *Petrology*, **165**, 757-779.
447 Foley, S.F., Barth, M.G. and Jenner, G.A. (2000) Rutile/melt partition coefficients for
448 trace elements and an assessment of the influence of rutile on the trace element
449 characteristics of subduction zone magmas. *Geochimica et Cosmochimica Acta*,
450 **64**, 933-938.
451 Gromet, L.P., Dymek, R.F., Haskin, L.A. and Korotev, R.L. (1984) The "North
452 American shale composite": Its composition, major and trace element
453 characterstics. *Geochimica et Cosmochimica Acta*, **48**, 2469-2482.
454 Hirtopanu, P., Fairhurst, R.J. and Jakab, G. (2015) Niobian rutile and its associations at
455 Jolotca, Ditrau alkaline intrusive massif, east Carpathians, Romania.
456 *Proceedings of Romania Academy*, **Series B, 17**, 39-55.
457 Kato, T. (2005) New accurate Bence-Albee α-factors for oxides and silicates
458 calculated from the PAP correction procedure. *Geostandrds and Geoanalytical*
459 *Research*, **29**, 83-94.
460 Khodos, M.Y., Belysheva, G.M. and Krivosheev, N.V. (1988) Solid solutions with the
461 rutile structure in the TiO_2-Nb_2O_5 system. *Russian Journal of Inorganic*
462 *Chemistry*, **33**, 604-606.
463 Klemme, S., Prowatke, S., Hametner, K. and Günther, D. (2005) Partitioning of trace
464 elements between rutile and silicate melts: Implications for subduction zones.
465 *Geochimica et Cosmochimica Acta*, **69**, 2361-2371.
466 Korolev, N.M., Marin, Y.B., Nikitina, L.P., Zinchenko, V.N. and Chissupa, H.M. (2014)
467 High-Nb rutile from upper mantle eclogite xenoliths of the diamond-bearing

kimberlite pipe Catoca (Angola). *Doklady Earth Sciences*, **454**, 50-53.

Luvizotto, G.L. and Zack, T. (2009) Nb and Zr behavior in rutile during high-grade metamorphism and retrogression: An example from the Ivrea-Verbano Zone. *Chemical Geology*, **261**, 303-317.

Luvizotto, G.L., Zack, T., Triebold, S. and von Eynatten, H. (2009) Rutile occurrence and trace element behavior in medium-grade metasedimentary rocks: example from the Erzgebirge, Germany. *Mineralogy and Petrology*, **97**, 233–249.

Maw Maw Win, Enami, M. and Kato, T. (2016) Metamorphic conditions and CHIME monazite ages of Late Eocene to Late Oligocene high-temperature Mogok metamorphic rocks in central Myanmar. *Journal of Asian Earth Sciences*, **117**, 304-316.

Meinhold, G. (2010) Rutile and its applications in earth sciences. *Earth-Science Reviews*, **102**, 1-28.

Meyer, M., John, T., Brandt, S. and Klemd, R. (2011) Trace element composition of rutile and the application of Zr-in-rutile thermometry to UHT metamorphism (Epupa Complex, NW Namibia). *Lithos*, **126**, 388-401.

Mitchell, A.H.G., Myint Thein Htay, Htun, K.M., Myint Naing Win, Thura Oo and Tin Hlaing. (2007) Rock relationships in the Mogok metamorphic belt, Tatkon to Mandalay, central Myanmar. *Journal of Asian Earth Sciences*, **29**, 891-910.

Oberti, R., Smith, D.C., Rossi, G. and Caucia, F. (1991) The crystal-chemistry of high-aluminium titanites. *European Journal of Mineralogy*, **3**, 777-792.

Pape, J., Mezger, K. and Robyr, M. (2016) A systematic evaluation of the Zr‐in‐rutile thermometer in ultra‐high temperature (UHT) rocks. *Contributions to Mineralogy and Petrology*, **171**, 44.

492 Rezvukhin, D.I., Malkovets, V.G., Sharygin, I.S., Kuzmin, D.V., Litasov, K.D., Gibsher,
493 A.A., Pokhilenko, N.P. and Sobolev, N.V. (2016) Inclusions of Cr- and
494 Cr-Nb-Rutile in pyropes from the Internatsionalnaya kimberlite pipe, Yakutia.
495 *Doklady Earth Sciences*, **466**, 173-176.
496 Searle, M.P., Noble, S.R., Cottle, J.M., Waters, D.J., Mitchell, A.H.G., Tin Hlaing and
497 Horstwood, M.S.A. (2007) Tectonic evolution of the Mogok metamorphic belt,
498 Burma (Myanmar) constrained by U-Th-Pb dating of metamorphic and
499 magmatic rocks. *Tectonics*, **26**, TC3014.
500 Smith, D.C. (1988) A review of the peculiar mineralogy of the "Norwegian-eclogite
501 province," with crystal-chemical, petrological, geochemical and geodynamical
502 notes and an extensive bibliography. Pp. 1-206. in: *Eclogites and*
503 *Eclogite-Facies Rocks* (D.C. Smith, editor). **12**, Elsevier, Amsterdam.
504 Smith, D.C. and Perseil, E.A. (1997) Sb-rich rutile in the manganese concentrations at
505 St. Marcel-Praborna, Aosta Valley, Italy: petrology and crystal-chemistry.
506 *Mineralogical Magazine*, **61**, 655-669.
507 Sobolev, N.V., Logvinova, A.M., Lavrent'ev, Y.G., Karmanov, N.S., Usova, L.V.,
508 Koz'menko, O.A. and Ragozin, A.L. (2011) Nb-rutile from eclogite
509 microxenolith of the Zagadochnaya kimberlite pipe. *Doklady Earth Sciences*,
510 **439**, 970-973.
511 Tan, W., Wang, C.Y., He, H., Xing, C., Liang, X. and Dong, H. (2015) Magnetite-rutile
512 symplectite derived from ilmenite-hematite solid solution in the Xinjie Fe-Ti
513 oxide-bearing, mafic-ultramafic layered intrusion (SW China). *American*
514 *Mineralogist*, **100**, 2348-2351.
515 Taylor, S.R. and McLennan, S.M. (1988) The significance of the rare earths in

geochemistry and cosmochemistry. Pp. 485-578. in: *Handbook on the Physics and Chemistry of Rare Earths* (K.A. Gschneider, Jr. and L. Eyring, editors). **11**, Elsevier, Amsterdam.

Tollo, R.P. and Haggerty, S.E. (1987) Nb-Cr-rutile in the Orapa kimberlite, Botswana. *Canadian Mineralogist*, **25**, 251-264.

Tomkins, H.S., Powell, R. and Ellis, D.J. (2007) The pressure dependence of the zirconium-in-rutile thermometer. *Journal of Metamorphic Geology*, **25**, 703-713.

Villaseca, C., Orejana, D. and Paterson, B.A. (2007) Zr–LREE rich minerals in residual peraluminous granulites, another factor in the origin of low Zr–LREE granitic melts? *Lithos*, 375-386.

Vlassopoulos, D., Rossman, G.R. and Haggerty, S.E. (1993) Coupled substitution of H and minor elements in rutile and the implications of high OH contents in Nb-and Cr-rich rutile from the upper mantle. *American Mineralogist*, **78**, 1181-1191.

Watson, E.B., Wark, D.A. and Thomas, J.B. (2006) Crystallization thermometers for zircon and rutile. *Contributions to Mineralogy and Petrology*, **151**, 413-433.

Yamamoto, K. and Morishita, T. (1997) Preparation of standard composites for trace element analysis by X-ray fluorescence. *Journal of Geological Society of Japan*, **103**, 1037-1045 (in Japanese with English abstract).

Ye Kyaw Thu, Maw Maw Win, Enami, M. and Tsuboi, M. (2016) Ti-rich biotite in spinel and quartz-bearing paragneiss and related rocks from the Mogok metamorphic belt, central Myanmar. *Journal of Mineralogical and Petrological Sciences*, **111**, 270-282.

Ye Kyaw Thu, Enami, M., Kato, T. and Tsuboi, M. (2017) Granulite facies paragneisses

from the middle segment of the Mogok metamorphic belt, central Myanmar. *Journal of Mineralogical and Petrological Sciences*, **112**, 1-19.

Yonemura, K., Osanai, Y., Nakano, N., Adachi, T., Charusiri, P. and Tun Naing Zaw. (2013) EPMA U-Th-Pb monazite dating of metamorphic rocks from the Mogok Metamorphic Belt, central Myanmar. *Journal of Mineralogical and Petrological Sciences*, **108**, 184-188.

Zack, T., Kronz, A., Foley, S.F. and Rivers, T. (2002) Trace element abundances in rutiles from eclogites and associated garnet mica schists. *Chemical Geology*, **184**, 97–122.

Zack, T., Moraes, R. and Kronz, A. (2004) Temperature dependence of Zr in rutile: empirical calibration of a rutile thermometer. *Contributions to Mineralogy and Petrology*, **148**, 471-488.

553 Captions for Tables

554 FIG. 1. Geologic maps of (a) Myanmar and adjacent regions showing major suture
555 zones, faults, and terrane boundaries (Searle *et al.*, 2007) and (b) central
556 Myanmar, showing sample localities (compiled from unpublished geological
557 data from Myint Thein).

558 FIG. 2. Back-scattered electron images showing the modes of occurrence of rutile: (a)
559 intergrowth grain in biotite (S26), (b) isolated grain in biotite (S22a), (c)
560 isolated grains in an aggregate of felsic phases (S28), and (d) isolated and
561 intergrowth grains in an aggregate of felsic phases (S28). "Nbf-Rt" indicates
562 Nb-free- and Fe-rich rutile discussed in the text. White spots and numbers in
563 (c) and (d) imply analytical points and Zr contents (ppm), respectively.
564 Abbreviations for the minerals are: Bt, biotite; Chl, chlorite; Ilm, ilmenite; Kfs,
565 K-feldspar; Mnz, monazite; Pl, plagioclase; Qz, quartz; Rt, rutile; and Zrn,
566 zircon. Lines A–A' and B–B' show the positions of the step-scan analyses of
567 Figs. 8 and 13, respectively.

568 FIG. 3. Cumulative diagram of Fe_2O_3 content (wt%) of rutile. "Nbf-Rt" indicates the
569 compositional range of aggregate of rutile grains included by ilmenite shown in
570 Fig. 2a. Abbreviations are: Fsi, rutile in felsic phases; and Bi, rutile in biotite.

571 FIG. 4. Cumulative diagram of Nb_2O_5 content (wt%) of rutile. "Nbf-Rt" indicates the
572 compositional range of aggregate of rutile grains included by ilmenite shown in
573 Fig. 2a. Abbreviations are: Fsi, rutile in felsic phases; Bi, rutile in biotite; and
574 D.L., detection limit (2σ level).

FIG.5. Compositional variations of V_2O_3 and Cr_2O_3 contents (wt%) of rutile. Abbreviations are: Fsi, rutile in felsic phases; Bi, rutile in biotite; and D.L., detection limit (2σ level).

FIG. 6. Histograms of Zr content (ppm) in rutile. Temperature calibration follows Tomkins *et al.* (2007). Some data from samples S22a, S22b, and S26 are from Fig. 6 of Maw Maw Win et al. (2016). Pressure conditions of the peak metamorphic stage of the Mogok belt were estimated as 0.6–1.0 GPa (Maw Maw Win *et al.*, 2016; Ye Kyaw Thu *et al.*, 2016, 2017), and, therefore the pressure condition was assumed to be 0.8 GPa for the temperature estimation. The pressure dependence of the Zr-in rutile geothermometer is small at about 50 °C/GPa in the pressure range less than 1.0 GPa.

FIG. 7. (a) TiKα, (b) NbLα, (c) AlKα, and (d) FeKα X-ray image maps of intergrowth grains of Nb-rich rutile and ilmenite occurring as an inclusion in biotite. "Nbf-Rt" indicates Nb-free- and Fe-rich rutile discussed in the text. A back-scattered electron image of this grain is shown in Fig. 2a. Abbreviations for minerals are: Bt, biotite; Ilm, ilmenite; and Rt, rutile. Line A–A' shows the position of the step-scan analysis of Fig. 8.

FIG. 8. Step-scan analysis of zoned Nb-rich rutile along the line A–A' shown in Figs. 2a and 7a.

FIG. 9. Relationship between M^{3+} and Nb' (= Nb -$2M^{2+}$) contents of the Nb-bearing rutile in sample S26 assuming iron as (a) Fe^{3+} and (b) Fe^{2+}, where M^{3+} and M^{2+} indicate the sums of the trivalent and divalent elements, respectively.

597 FIG. 10. Relationship between Ti and Nb" (= Nb + M^{3+}) contents of the Nb-bearing
598 rutile in sample S26 assuming total iron as Fe^{3+}, where M^{3+} indicates the sum
599 of the trivalent elements.
600 FIG 11. Relationship between Ti and iron contents of Nb-free and Fe-rich rutile in
601 sample S26 assuming total iron as (a) Fe^{3+} and (b) Fe^{2+}, respectively.
602 FIG. 12. Compositional ranges of biotite grains with and without rutile inclusions in
603 sample S22a.
604 FIG. 13. Step-scan analysis of Ti-rich biotite surrounding a rutile inclusion (S22a) along
605 line B–B' shown in Fig. 2b.

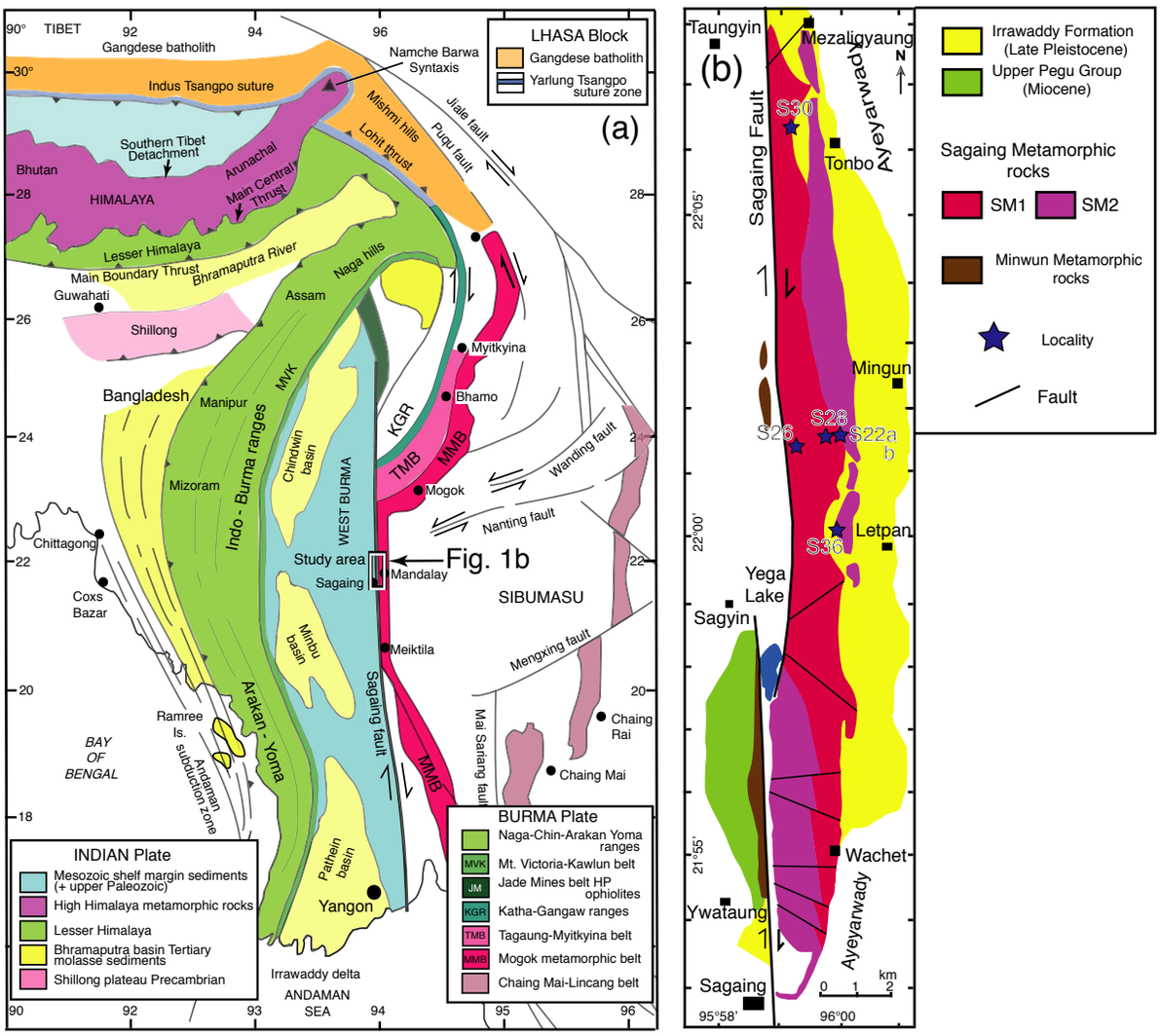

FIG. 1. Geologic maps of (a) Myanmar and adjacent regions showing major suture zones, faults, and terrane boundaries (Searle et al., 2007) and (b) central Myanmar, showing sample localities (compiled from unpublished geological data from Myint Thein).

Maw Maw Win and others (Fig.01)

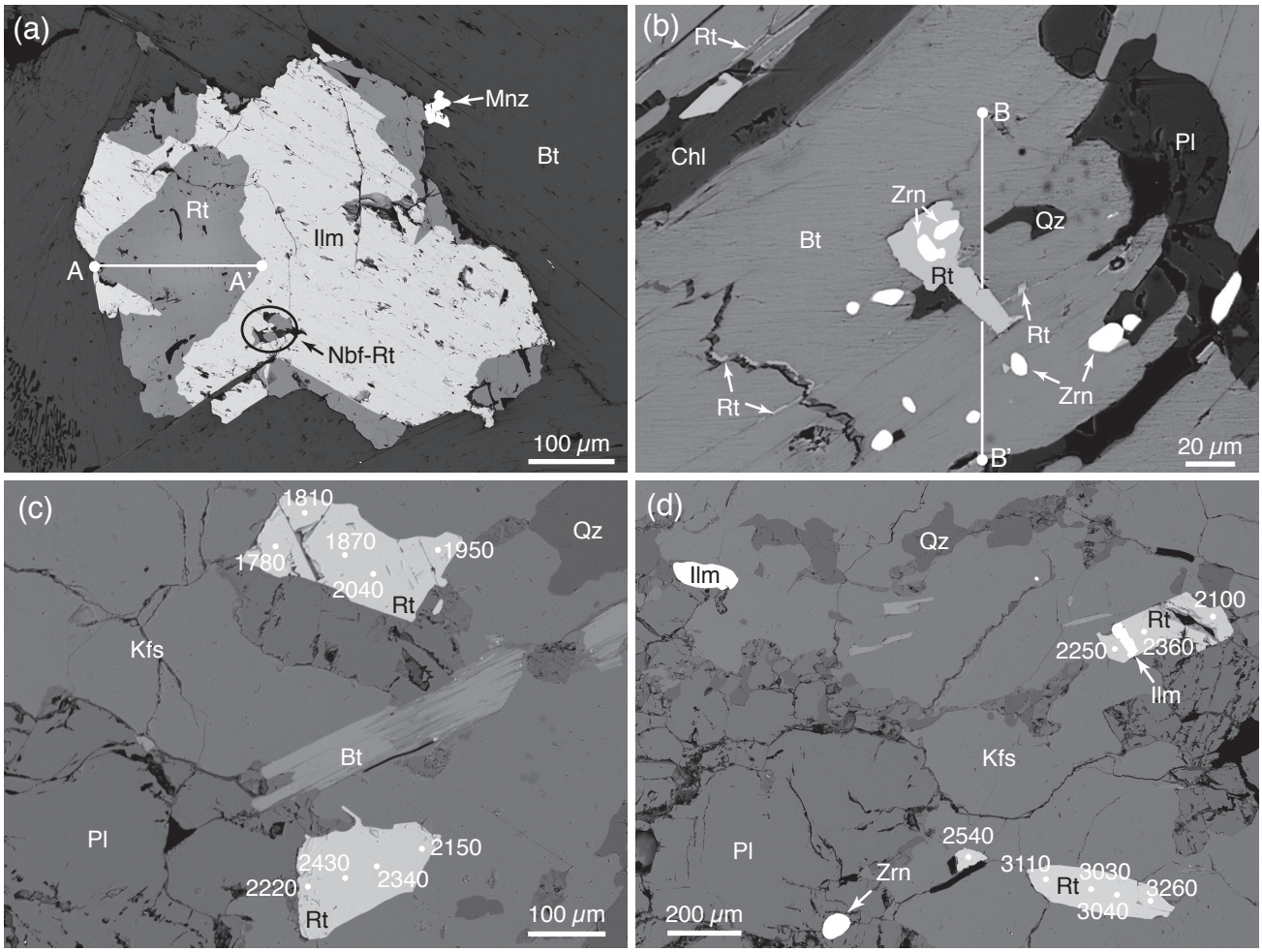

FIG. 2. Back-scattered electron images showing the modes of occurrence of rutile: (a) intergrowth grain in biotite (S26), (b) isolated grain in biotite (S22a), (c) isolated grains in an aggregate of felsic phases (S28), and (d) isolated and intergrowth grains in an aggregate of felsic phases (S28). “Nbf-Rt” indicates Nb-free- and Fe-rich rutile discussed in the text. White spots and numbers in (c) and (d) imply analytical points and Zr contents (ppm), respectively. Abbreviations for the minerals are: Bt, biotite; Chl, chlorite; Ilm, i lmenite; Kfs, K-feldspar; Mnz, monazite; Pl, plagioclase; Qz, quartz; Rt, rutile; and Zrn, zircon. Lines A–A' and B–B' show the positions of the step-scan analyses of Figs. 8 and 13, respectively.

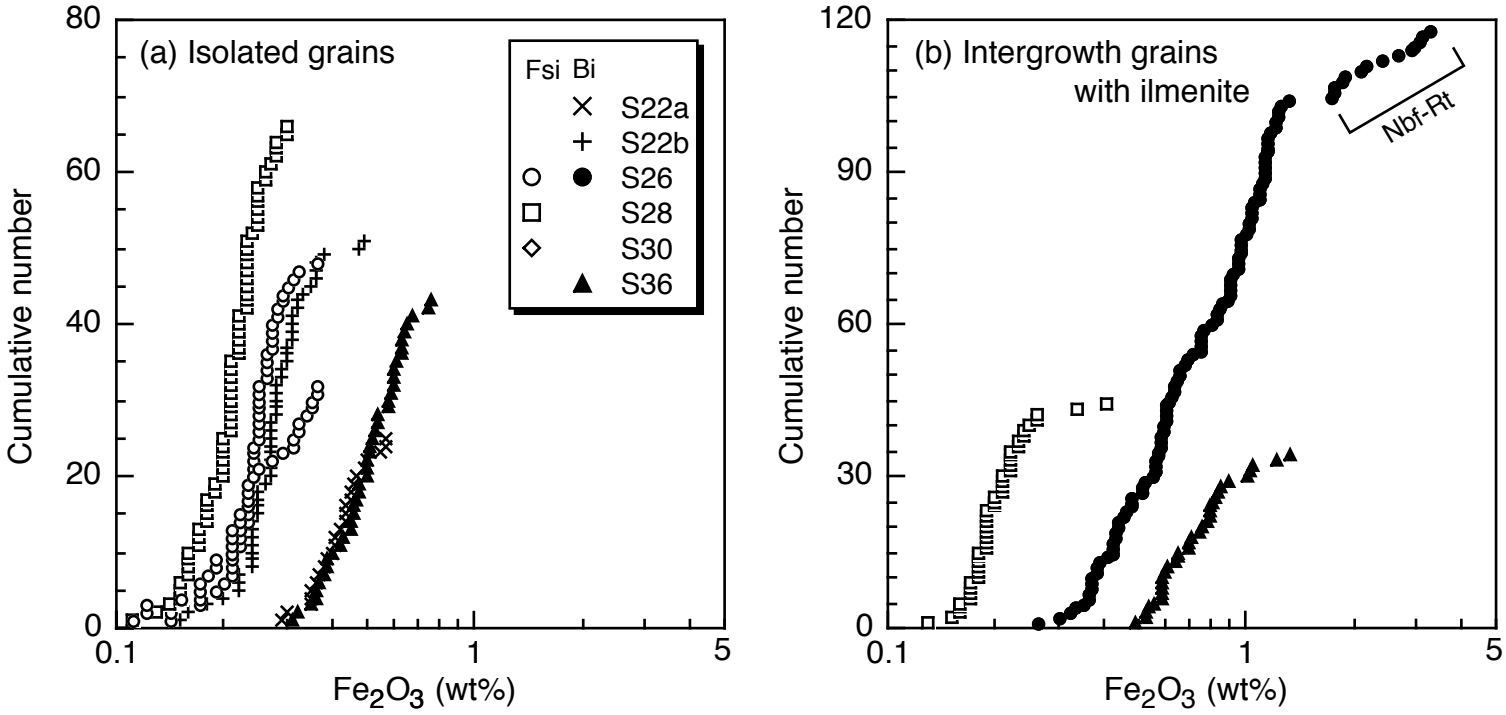

FIG. 3. Cumulative diagram of Fe2O3 content (wt%) of rutile. “Nbf-Rt” indicates the compositional range of aggregate of rutile grains included by ilmenite shown in Fig. 2a. Abbreviations are: Fsi, rutile in felsic phases; and Bi, rutile in biotite.

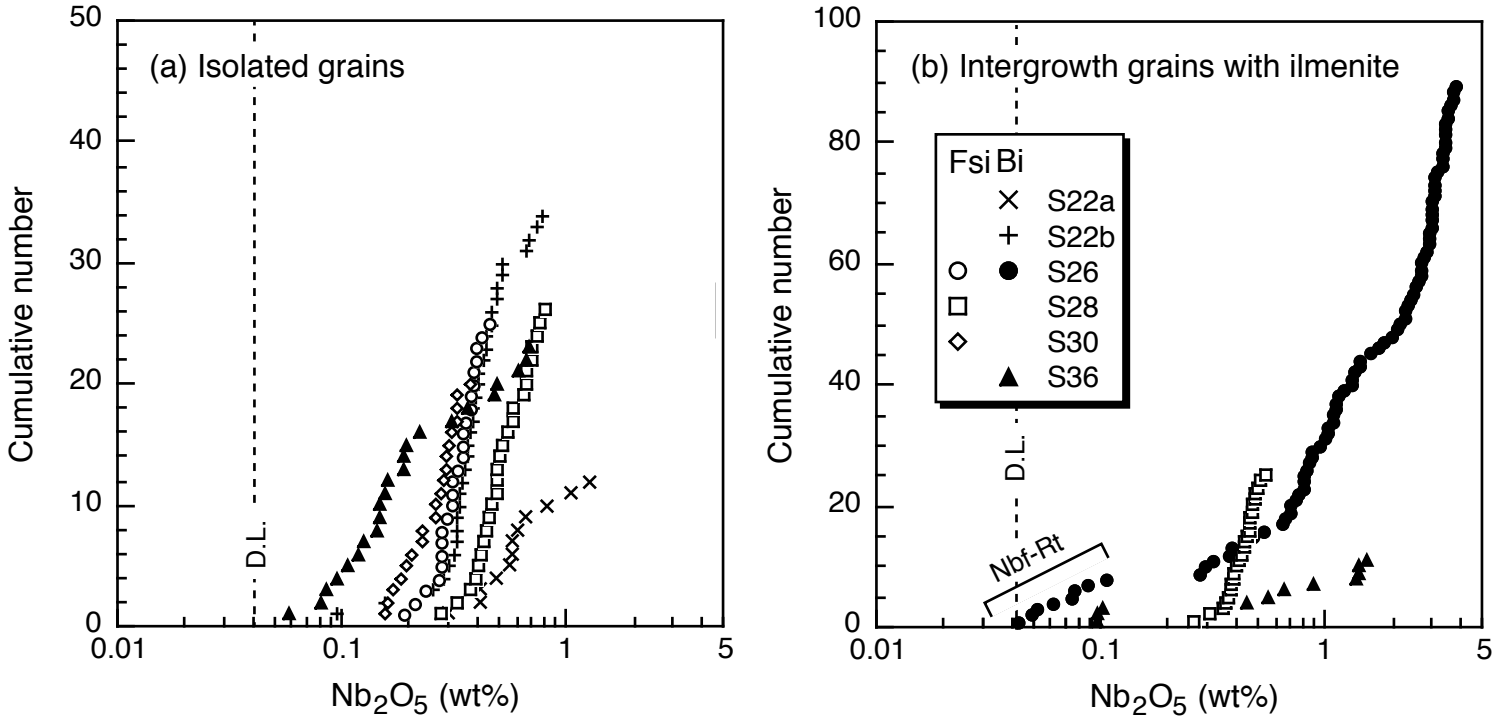

FIG. 4. Cumulative diagram of Nb_2O_5 content (wt%) of rutile. “Ndf-Rt” indicates the compositional range of aggregate of rutile grains included by ilmenite shown in Fig. 2a. Abbreviations are: Fsi, rutile in felsic phases; Bi, rutile in biotite; D.L., detection limit (2σ level).

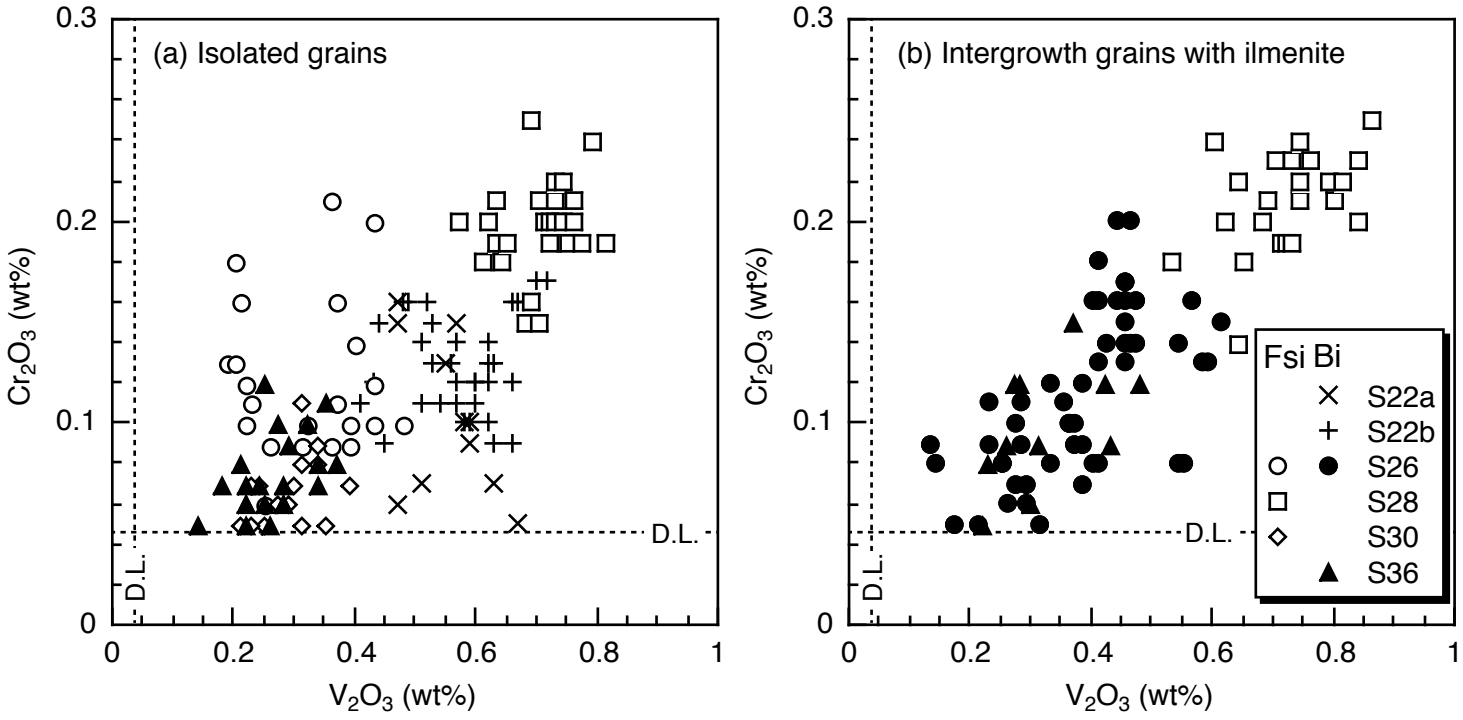

FIG.5. Compositional variations of V_2O_3 and Cr_2O_3 contents (wt%) of rutile. Abbreviations are: Fsi, rutile in felsic phases; Bi, rutile in biotite; D.L., detection limit (2σ level).

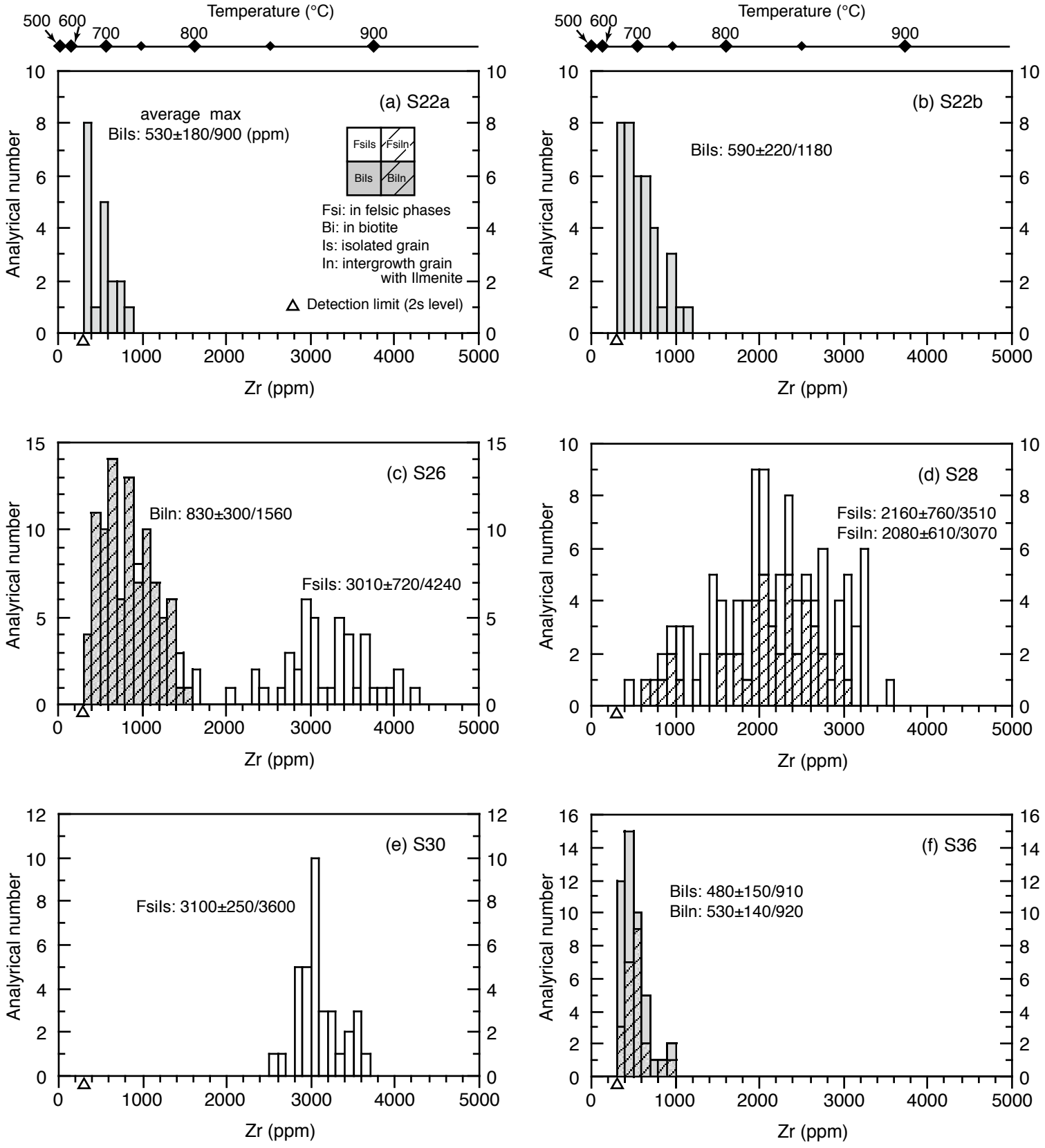

FIG. 6. Histograms of Zr content (ppm) in rutile. Temperature calibration follows Tomkins et al. (2007). Some data of samples S22a, b and S26 are from Fig. 6 of Maw Maw Win et al. (2016). Pressure conditions of peak metamorphic stage of the Mogok belt were estimated as 0.6–1.0 GPa (Maw Maw Win et al., 2016; Ye Kyaw Thu et al., 2016, 2017), and thus, pressure condition was assumed to be 0.8 GPa for the temperature estimation. The pressure dependence of the Zr-in rutile geothermometer is little of about 50 °C/GPa in the pressure range less than 1.0 GPa.

Maw Maw Win and others (Fig.06)

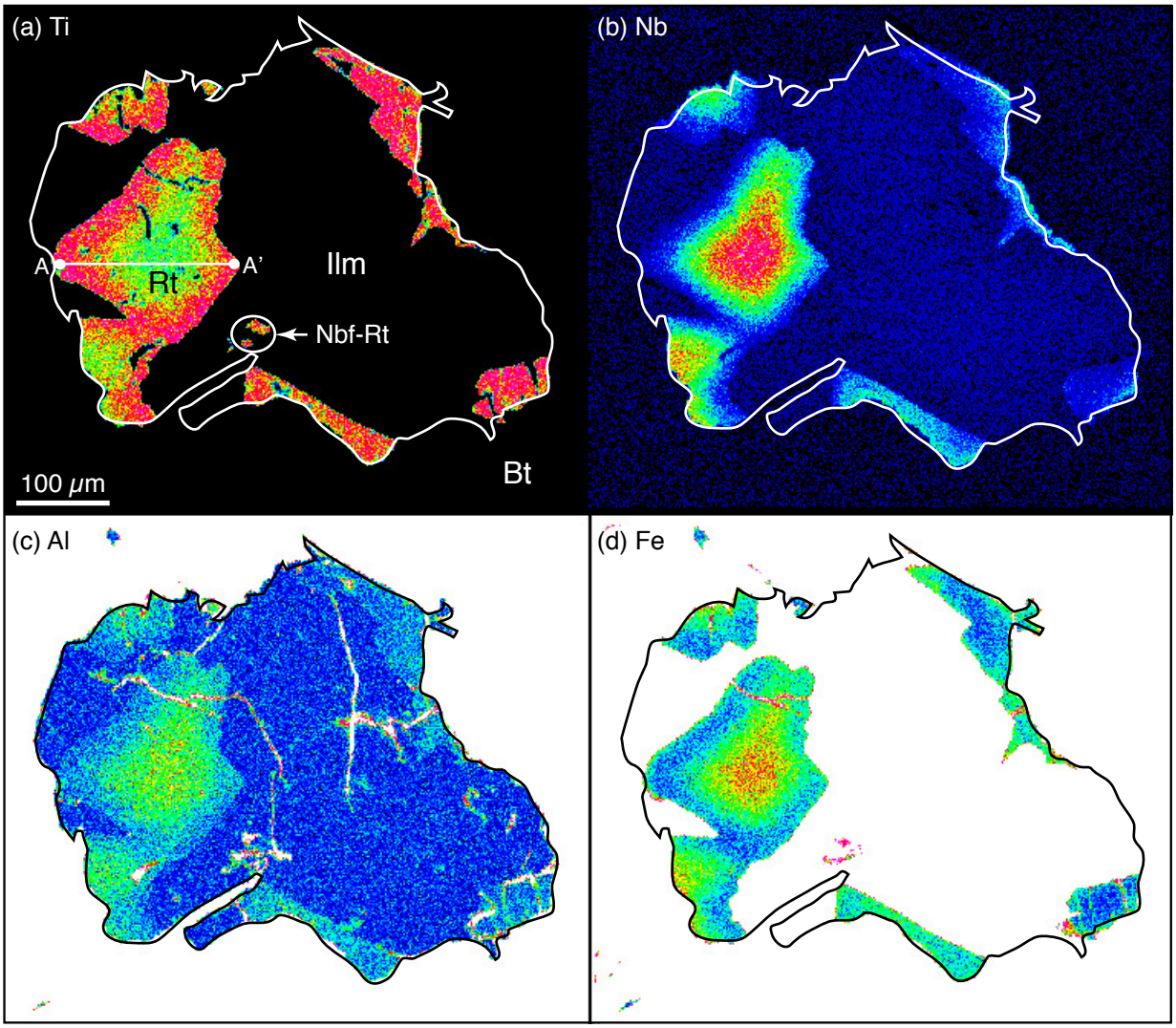

FIG. 7. (a) TiKα, (b) NbLα, (c) AlKα, and (d) FeKα X-ray image maps of intergrowth grains of Nb-rich rutile and ilmenite occurring as an inclusion in biotite. “Nbf-Rt” indicates Nb-free- and Fe-rich rutile discussed in the text. Back-scattered electron image of this grain is shown in Fig. 2a. Abbreviations for minerals are: Bt, biotite; Ilm, ilmenite; Rt, rutile. Line A–A' shows the position of the step-scan analysis of Fig. 8.

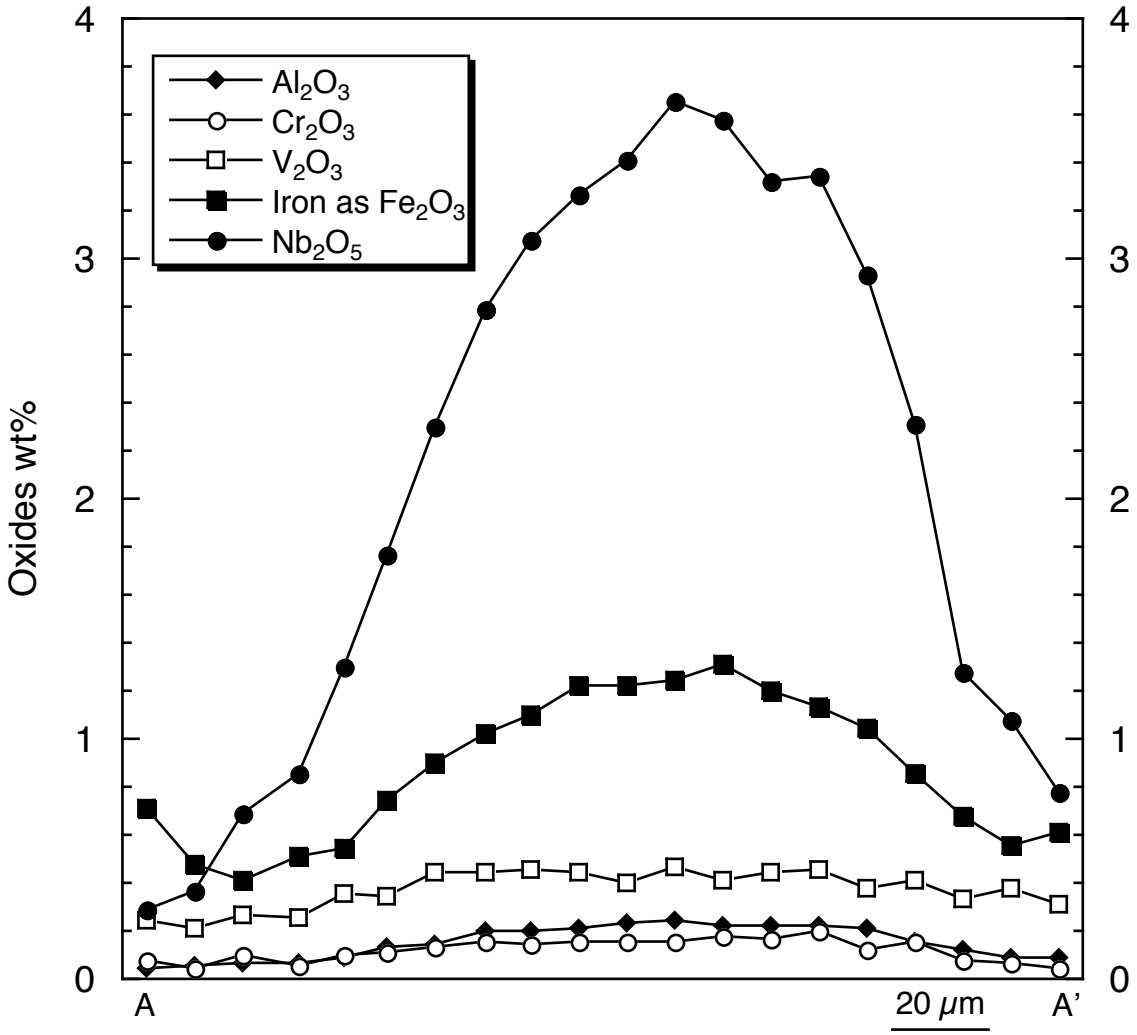

FIG. 8. Step-scan analysis of zoned Nb-rich rutile along the line A–A' shown in Figs. 2a and 7a.

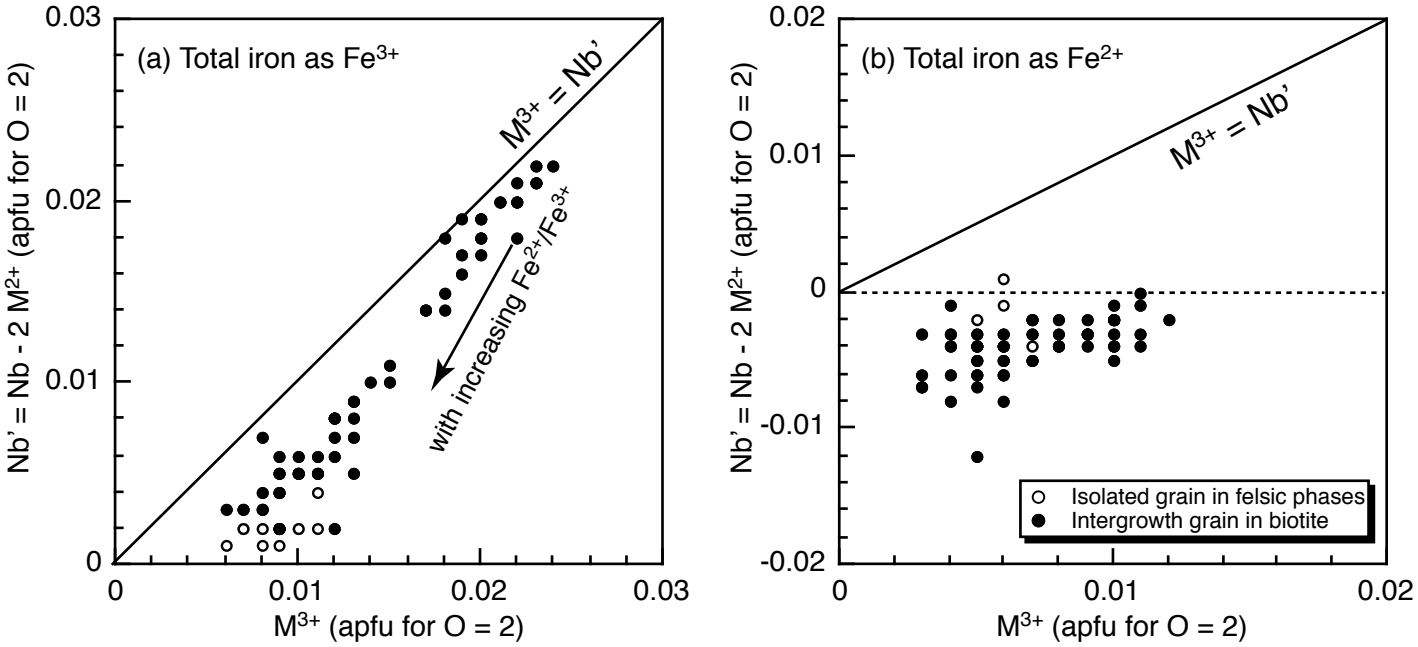

FIG. 9. Relationships between M^{3+} and Nb' (= Nb -2M^{2+}) contents of the Nb-bearing rutile in sample S26 assuming iron as (a) Fe^{3+} and (b) Fe^{2+}, where M^{3+} and M^{2+} indicate the sums of the trivalent and divalent elements, respectively.

Maw Maw Win and others (Fig.09)

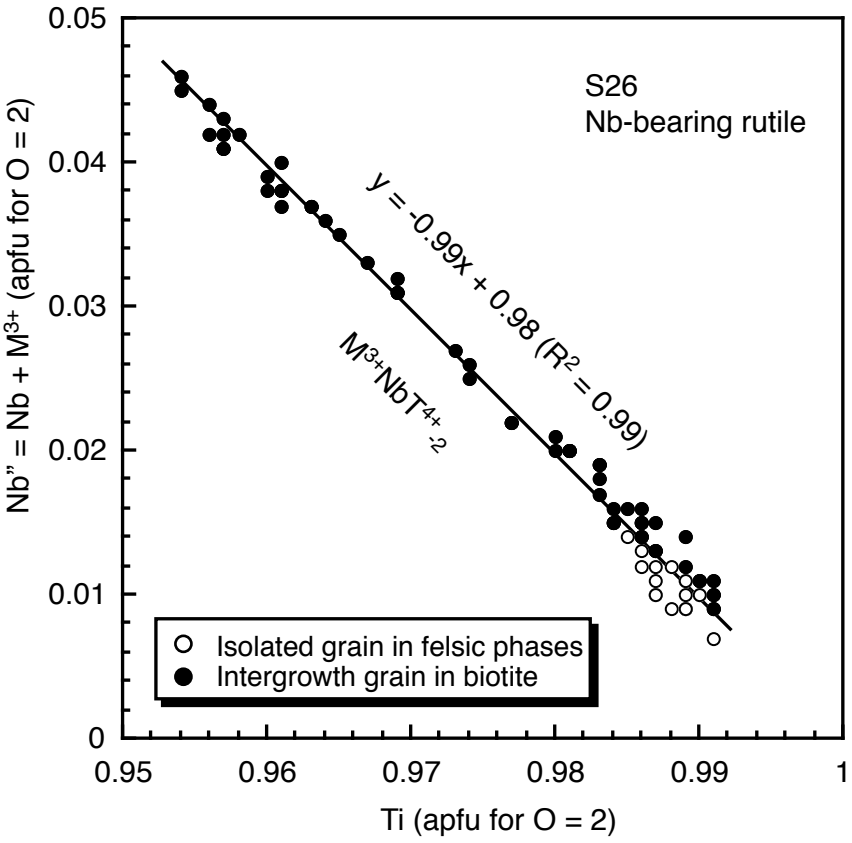

FIG. 10. Relationships between Ti and Nb" (= Nb + M^{3+}) contents of Nb-bearing rutile in sample S26 assuming total iron as Fe^{3+}, where M^{3+} indicates the sum of the trivalent elements.

Maw Maw Win and others (Fig.10)

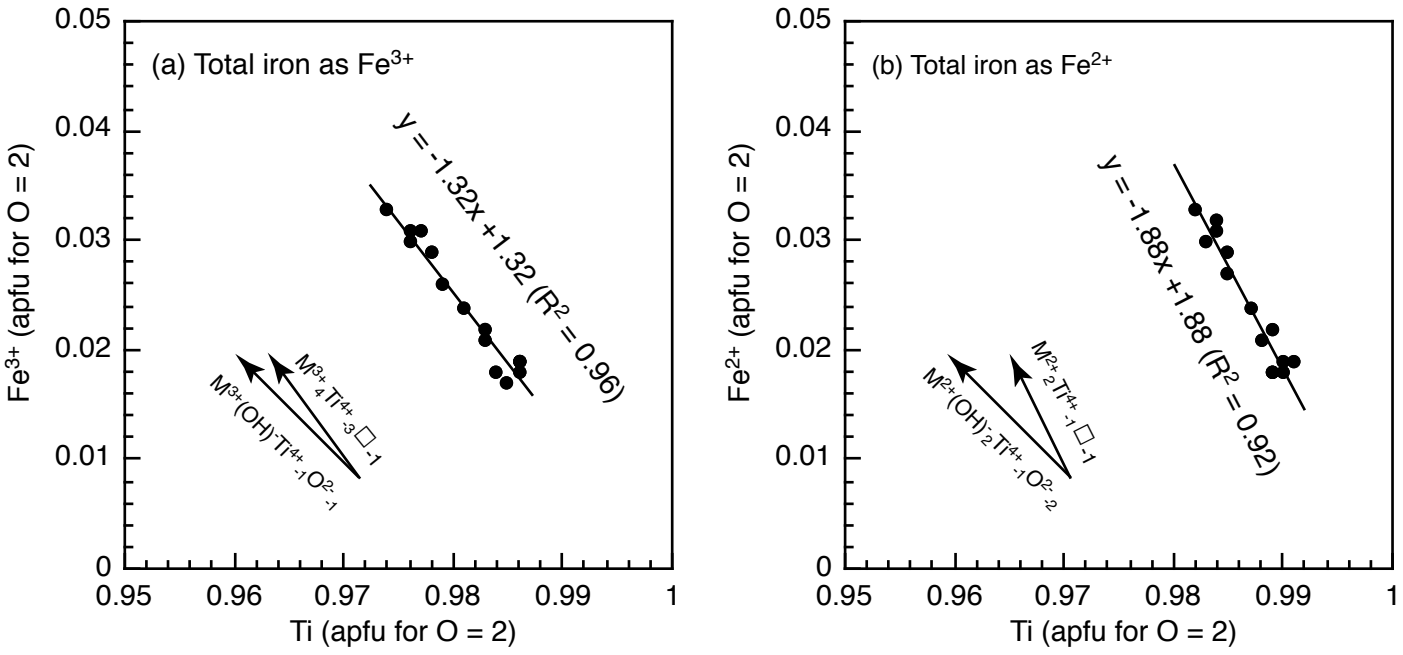

FIG 11. Relationships between Ti and iron contents of Nd-free and Fe-rich rutile in sample S26 assuming total iron as as (a) Fe^{3+} and (b) Fe^{2+}, respectively.

Maw Maw Win and others (Fig.11)

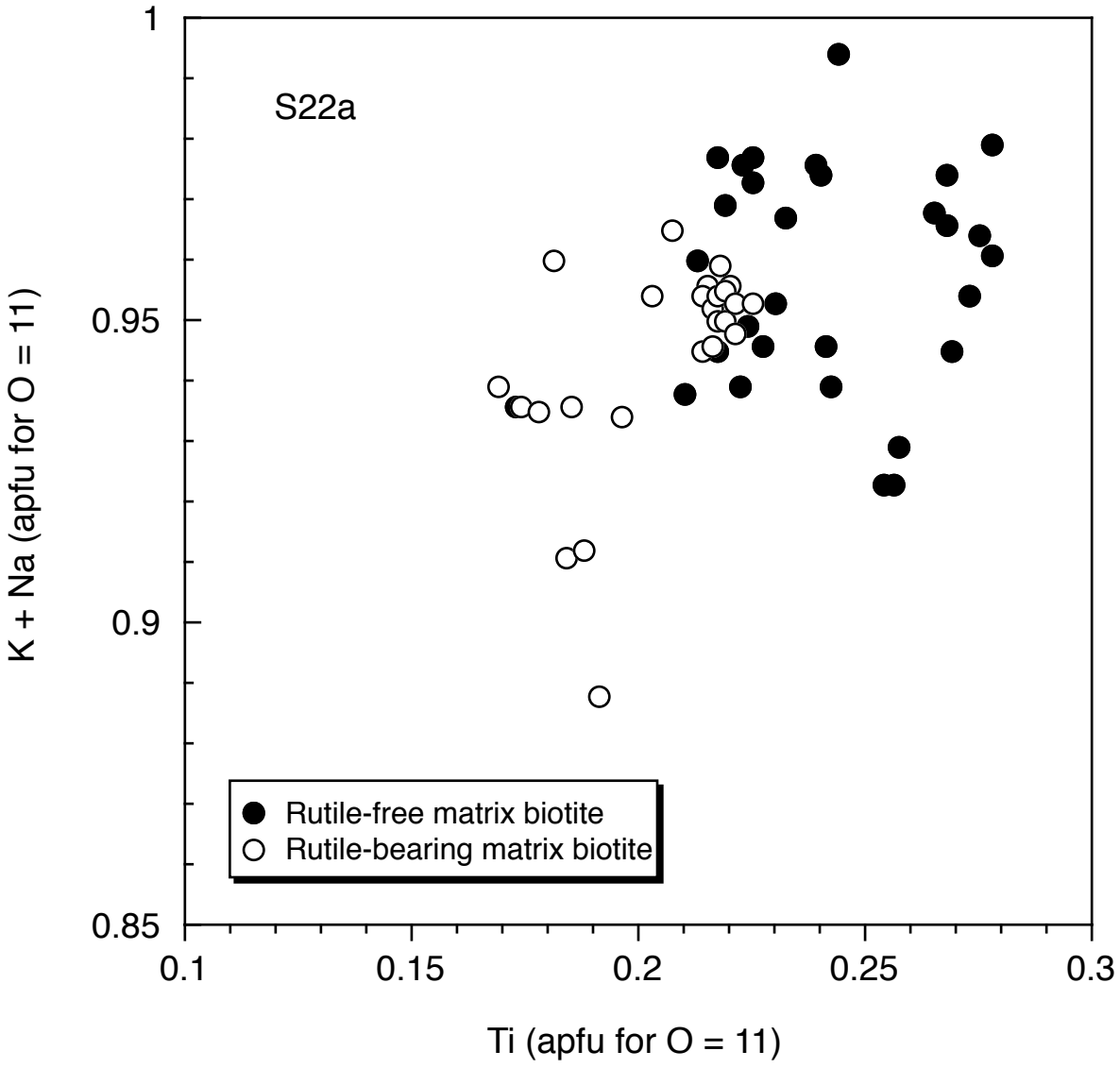

FIG. 12. Compositional ranges of biotite grains with and without rutile inclusion in sample S22a.

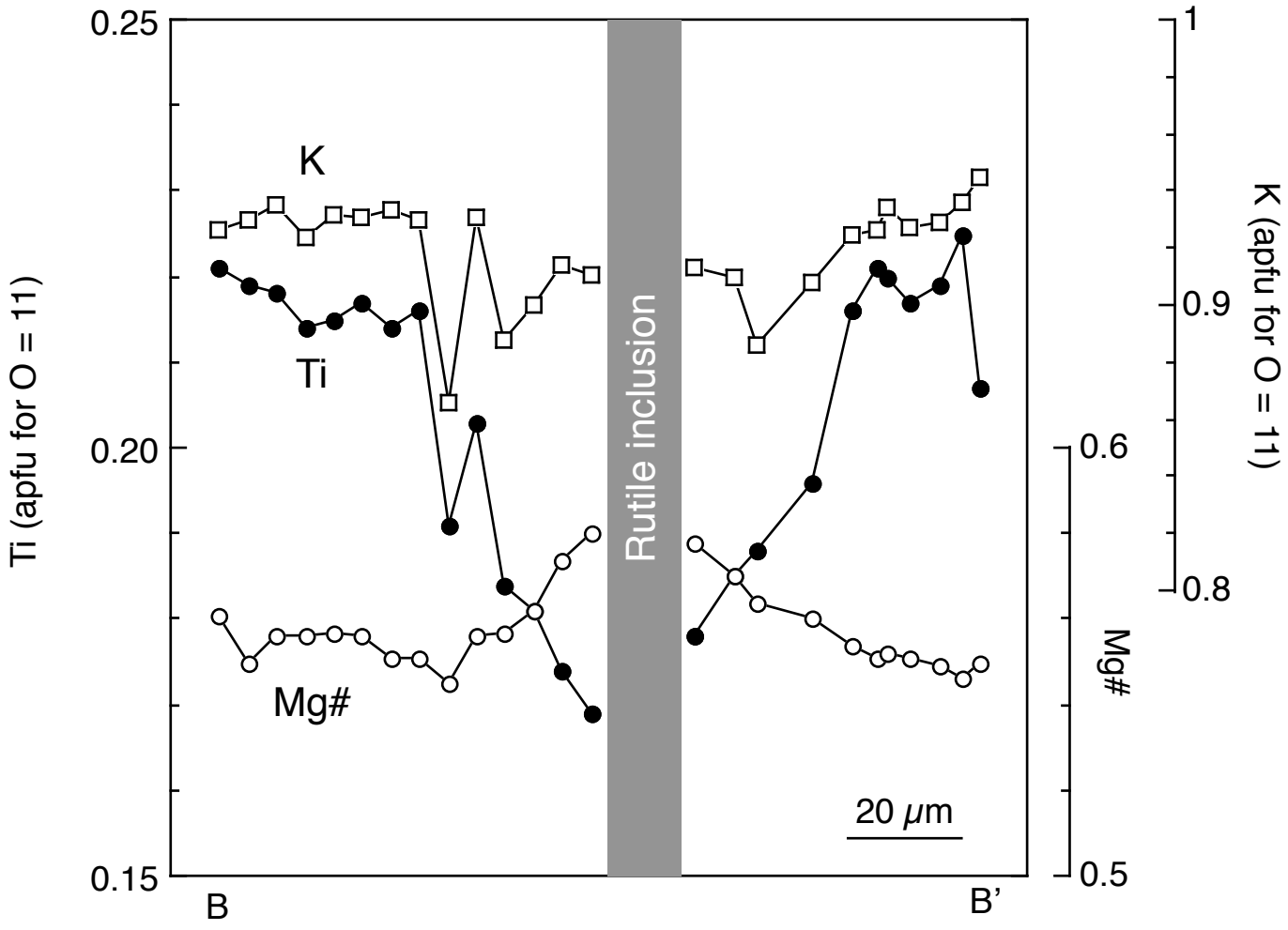

FIG. 13. Step-scan analysis of Ti-rich biotite surrounding a rutile inclusion (S26) along the line B–B' shown in Fig. 2b.

Table 1. Mineral assemblages of Sagaing paragneisses of the Mogok metamorphic belt, central Myanmar

Sample	Unit	Grt	Bt*	Pl**	Kfs	Qz	Sil	Ms	Rt	Ilm	Gr	Ap	Mnz	Zrn
S22a	2	+	5.0	44	+	+	g		b		+	+	+	+
S22b	2	+	6.2	48	+	+	g		b		+	+	+	+
S26	1	+	5.3	59	+	+	g, m		b, f	+	+	+	+	+
S28	1	+	4.4	49	+	+	g		f	+	+	+	+	+
S30	1	+	4.0	35	+	+	g, m	s	f	+	+	+	+	+
S36	2	+	4.1	50	+	+	m		b	+	+	+	+	+

* Maximum TiO_2 content (wt%).
** Anorthite content of calcic core.
Abbreviations are: Grt, garnet; Bt, biotite; Pl, plagioclase; Kfs, K-feldspar; Qz, quartz; Sil, sillimanite; Ms, muscovite; Rt, rutile; Ilm, ilmenite; Gr, graphite; Ap, apatite; Mnz, monazite; Zrn, zircon; +, present; g, inclusion in garnet; m, matrix phase; s, secondary phase replacing sillimanite; b, inclusion in biotite; f, inclusion in felsic phases.

Table 2. Whole-rock compositions of paragneisses of the Mogok metamorphic belt, central Myanmar

Sample	S22a	S22b	S26	OZ04b†
Unit	2	2	1	
Locality	Sagaing	Sagaing	Sagaing	Onzon
(wt%)				
SiO_2	67.45	62.58	51.73	69.99
TiO_2	0.67	0.80	1.32	0.84
Al_2O_3	12.58	14.90	18.61	12.38
FeO*	7.12	7.14	11.87	5.70
MnO	0.14	0.11	0.19	0.09
MgO	3.17	3.28	5.51	3.48
CaO	1.46	1.45	2.33	1.34
Na_2O	1.46	1.15	1.42	1.76
K_2O	3.52	5.86	3.42	2.35
P_2O_5	0.05	0.10	0.10	0.07
LOI**	2.39	1.07	1.44	0.77
Total	100.01	98.44	97.95	98.77
(ppm)				
Cr	97	96	195	123
Co	17	19	30	20
Ni	31	33	57	54
Cu	7	7	37	162
Zn	67	92	163	71
Ga	13	17	22	17
Rb	120	249	149	108
Sr	305	158	181	89
Y	58	48	77	38
Zr	279	232	272	279
Nb	18	17	29	13
Ba	900	883	635	358
Rb	22	40	33	14
Th	35	32	65	21

* Total iron as FeO.

** Loss on ignition.

† Paragneiss from the Onzon area (Ye Kyaw Thu *et al.*, 2017).

Table 3. Representative analyses of rutile and ilmenite in Sagaing paragneisses from the Mogok metamorphic belt, central Myanmar

Sample	S22a	S22b	S26				
Host	Bt	Bt	Fsc	Bt			
Mineral	Rt	Rt	Rt	Rt			Ilm
Texture	Iso	Iso	Iso	Int	Int	Int	Int
Position	core	core	core	core	rim	Nbf	
EPMA	733	733	733	8800	8800	8800	8800
(wr%)							
SiO_2				0.07	bd	bd	0.03
TiO_2	97.16	97.88	97.79	93.69	98.69	96.56	52.01
Al_2O_3	0.27	0.05	0.05	0.24	0.04	bd	bd
Cr_2O_3	bd	0.14	0.10	0.16	0.08	bd	0.07
V_2O_3	0.50	0.50	0.48	0.47	0.25	0.09	0.10
Fe_2O_3*	0.55	0.31	0.32	1.24	0.71	3.23	
FeO**							46.88
MnO	bd	bd	bd	0.03	bd	bd	0.42
MgO	bd	bd	bd	bd	bd	bd	0.61
Nb_2O_5	1.26	0.46	0.27	3.66	0.28	bd	0.04
Ta_2O_5	bd	bd	bd				
ZrO_2	0.07	0.09	0.55	0.14	0.08	bd	bd
Total	99.81	99.43	99.56	99.70	100.19	99.88	100.16
Zr (ppm)	520	670	4070	1040	590		
Formulae							
O	2	2	2	2	2	2	3
Si				0.001			0.001
Ti	0.979	0.988	0.987	0.953	0.989	0.975	0.981
Al	0.004	0.001	0.001	0.004	0.001		
Cr		0.001	0.001	0.002	0.001		0.001
V	0.005	0.005	0.005	0.005	0.003	0.001	0.002
Fe^{3+}*	0.006	0.003	0.003	0.013	0.007	0.033	0.032†
Fe^{2+}**							0.951†
Mn							0.009
Mg							0.023
Nb	0.008	0.003	0.002	0.022	0.002		0.000
Ta							
Zr	0.000	0.001	0.004	0.001	0.001		
Total	1.002	1.002	1.003	1.001	1.004	1.009	2.000

* Total iron as Fe_2O_3.

** Total iron as FeO.

† Calculated values assuming stoichiometry.

Abbreviations are: Bt, biotite; Fsc, felsic phases; Grt, garnet; Rt, rutile; Ilm, ilmenite; Iso, isolated grain; Int, Intergrowth grain; Nbf, Nb-free and Fe-rich part; 733, JCXA-733; 8800, JCXA-8800R; bd, below detection limit.

Table 3. (continuted)

Sample	S28			S30			S36	
Host	Fsc			Fsc		Grt	Bt	
Mineral	Rt	Rt	Ilm	Rt	Ilm	Ilm	Rt	Ilm
Texture	Iso	Int	Int	Int	Iso	Iso	Iso	Int
Position	core	core	core	core	core	core	core	
EPMA	8800	8800	8800	8800	8800	8800	8800	8800
(wr%)								
SiO_2	bd	0.03	bd	0.06	0.05	0.04	0.04	0.06
TiO_2	98.63	98.73	52.44	98.13	50.47	52.18	97.09	52.10
Al_2O_3	0.03	0.04	bd	0.05	bd	bd	0.05	bd
Cr_2O_3	0.25	0.25	bd	bd	bd	bd	0.12	0.04
V_2O_3	0.69	0.86	0.14	0.26	0.12	0.15	0.42	0.12
Fe_2O_3*	0.19	0.18		0.25			0.85	
FeO**			46.72		46.37	46.06		44.87
MnO	bd	bd	0.56	bd	0.26	0.50	0.04	1.73
MgO	0.02	0.02	0.57	bd	1.81	0.20	bd	0.14
Nb_2O_5	0.50	0.38	bd	0.20	bd	bd	1.52	0.13
Ta_2O_5	bd	bd		bd	bd			
ZrO_2	0.41	0.13	bd	0.49	bd	bd	0.12	bd
Total	100.72	100.62	100.43	99.44	99.08	99.13	100.25	99.19
Zr (ppm)	3040	960		3630			890	
Formulae								
O	2	2	3	2	3	3	2	3
Si		0.000		0.001	0.001	0.001	0.001	0.002
Ti	0.984	0.985	0.987	0.990	0.951	0.998	0.976	0.996
Al	0.000	0.001	bd	0.001	bd	bd	0.001	bd
Cr	0.003	0.003	bd	bd	bd	bd	0.001	0.001
V	0.007	0.009	0.003	0.003	0.002	0.003	0.004	0.002
Fe^{3+}*	0.002	0.002	0.024†	0.003	0.092†	0.000†	0.009	0.000†
Fe^{2+}**			0.953†		0.880†	0.979†		0.954†
Mn			0.012		0.006	0.011	0.000	0.037
Mg	0.000	0.000	0.021	0.000	0.068	0.008	bd	0.005
Nb	0.003	0.002		0.001			0.009	0.001
Ta								
Zr	0.003	0.001		0.003			0.001	
Total	1.002	1.003	2.000	1.002	2.000	2.000	1.002	1.998